Journal of Astronomical Telescopes, Instruments, and Systems

AstronomicalTelescopes.SPIEDigitalLibrary.org

Phase-induced amplitude apodization complex mask coronagraph mask fabrication, characterization, and modeling for WFIRST-AFTA

Brian Kern
Olivier Guyon
Ruslan Belikov
Daniel Wilson
Richard Muller
Erkin Sidick
Bala Balasubramanian
John Krist
Ilya Poberezhskiy
Hong Tang

SPIE.

Phase-induced amplitude apodization complex mask coronagraph mask fabrication, characterization, and modeling for WFIRST-AFTA

Brian Kern,[a,*] Olivier Guyon,[b,c] Ruslan Belikov,[d] Daniel Wilson,[a] Richard Muller,[a] Erkin Sidick,[a] Bala Balasubramanian,[a] John Krist,[a] Ilya Poberezhskiy,[a] and Hong Tang[a]
[a]Jet Propulsion Laboratory, California Institute of Technology, 4800 Oak Grove Drive, Pasadena, California 91016, United States
[b]University of Arizona, Department of Astronomy and Steward Observatory, 933 North Cherry Avenue, Tucson, Arizona 85721, United States
[c]Subaru Telescope, National Astronomical Observatory of Japan, 650 North A'ohoku Place, Hilo 96720, United States
[d]NASA Ames Research Center, Moffett Field, California 94035, United States

Abstract. This work describes the fabrication, characterization, and modeling of a second-generation occulting mask for a phase-induced amplitude apodization complex mask coronagraph, designed for use on the WFIRST-AFTA mission. The mask has many small features (~micron lateral scales) and was fabricated at the Jet Propulsion Laboratory Microdevices Laboratory, then characterized using a scanning electron microscope, atomic force microscope, and optical interferometric microscope. The measured fabrication errors were then fed to a wavefront control model which predicts the contrast performance of a full coronagraph. The expected coronagraphic performance using this mask is consistent with observing ~15 planetary targets with WFIRST-AFTA in a reasonable time (<1 day/target). [DOI: 10.1117/1.JATIS.2.1.011014]

Keywords: coronagraph; exoplanets; wavefront control.

Paper 15032SS received Jun. 1, 2015; accepted for publication Dec. 22, 2015; published online Jan. 28, 2016.

1 Introduction

There are currently three coronagraph technologies being developed/considered for the WFIRST-AFTA coronagraph.[1] One of these three technologies is a phase-induced amplitude apodization complex mask coronagraph (PIAACMC).[2] PIAACMC is similar to the PIAA coronagraph concept that has been tested at the Jet Propulsion Laboratory's (JPL's) high-contrast imaging testbed (HCIT),[3,4] with demonstrated results at 10^{-8} contrast in a 10% bandpass with a $2\lambda/D$ inner working angle (IWA), that are encouraging for space mission applications. PIAACMC differs from the earlier PIAA concept by adding a phase-only occulting mask, which allows for much smaller IWAs and much milder PIAA aspheric mirror shapes. The potential science yield from a PIAACMC implementation on WFIRST-AFTA is quite large,[5] but the PIAACMC concept has not yet been demonstrated at high contrasts, and so entails some technical risk in the WFIRST-AFTA planning. The mitigation of this risk begins with the fabrication and characterization of a PIAACMC occulting mask.

The WFIRST-AFTA Study Office created WFIRST-AFTA Coronagraph Milestones to track the technology maturation of the coronagraph concepts and components, in agreement with NASA Headquarters, and the fabrication and characterization of the PIAACMC occulting mask was highlighted in Milestone 3. The milestone was summarized as, "First-generation PIAACMC focal plane phase mask with at least 12 concentric rings has been fabricated and characterized; results are consistent with model predictions of 10^{-8} raw contrast with 10% broadband light centered at 550 nm." This one-sentence summary described only 10^{-8} raw contrast, while further specification was implied by a more detailed description in terms of the science goals of the mission, specifically the number of planets that can be observed given the demonstrated performance. The relevant requirement is to be able to observe at least 12 planets, reaching a signal-to-noise ratio (SNR) of five in under 1 day each. This work was presented to and approved by WFIRST-AFTA Coronagraph Technical Analysis Committee (TAC) as a successful accomplishment of the milestone.

2 Phase-Induced Amplitude Apodization Complex Mask Coronagraph on WFIRST-AFTA

PIAACMC is the backup architecture on WFIRST-AFTA, while the occulting mask coronagraph (OMC) is the primary architecture.[1] The existing baseline optical layouts are for the OMC configuration, which are not directly compatible with PIAACMC because PIAACMC uses a pair of aspheric mirrors to apodize the input beam. These aspheric mirrors cannot be used with the OMC layout, so the PIAACMC flight layout is necessarily different from the OMC layout.

The PIAACMC design discussed here is referred to as "Gen 2," to differentiate it from the design originally proposed for WFIRST-AFTA in November 2013.[6] Krist and Nemati[6] refer to the original design as the "downselect" design, and analyze a more recent "Gen 3" iteration, but do not consider the Gen 2 design described here. The optical layout specific to Gen 2 PIAACMC was chosen to use only a single deformable mirror (DM), to operate without pupil relay optics, and to illuminate the

*Address all correspondence to: Brian Kern, E-mail: Brian.D.Kern@jpl.nasa.gov

2329-4124/2016/$25.00 © 2016 SPIE

occulter plane with an F/80 beam (a very slow system). In addition, the Gen 2 PIAACMC occulter is entirely reflective, as contrasted with the transmissive OMC occulters. Being reflective, the PIAACMC occulter generates no internal reflections (ghosts), and is not sensitive to refractive property inhomogeneities. For a given occulter phase pattern, choosing a reflective design makes the physical features shallower by a factor of 4, compared to propagation through a material with the index of refraction ~1.5.

An illustration of the PIAACMC optical layout is shown in Fig. 1. The entire layout fits comfortably inside the 1 m × 1 m nominal instrument outline. The configuration of the optics feeding the instrument is subject to design revisions ("Cycle 4" is shown), but there should be no particular complications adapting this basic layout to changes in the surrounding components.

The choice to use only a single DM was made to simplify the instrument, as each DM and its electronics add cost and complexity, in addition to simple mass and power, to the instrument. Using a single DM typically restricts the high-contrast coronagraph field-of-view (FOV) to half of the image plane. Wavefront control with high contrast over a full 360-deg FOV typically requires two DMs. All analysis presented here is for wavefront control over only half of the image plane.

To categorize the optical differences between PIAACMC and OMC, there are three noteworthy components: the aspheric PIAA mirrors, the reflective PIAA occulting mask, and the elongated Lyot stop. The PIAA mirrors for Gen 2 have significantly milder aspheric shapes than for previous PIAA designs. The mirror surfaces differ from conic surfaces by only 2.1 μm $P-V$, as compared with 50 μm on previously fabricated PIAA mirrors used for high-contrast testbed demonstrations.[3] Figure 2 shows the difference between the surfaces of the Gen 2 mirrors with respect to simple conic surfaces.

The Lyot stop is a single component physically, but is not contained in a single plane. It can either be implemented as a small fixture (~30 mm deep) containing 3 to 4 planes of stops, or as a single elongated shape. A final decision on this construction must fold in consideration of the LOWFS optical arrangement for PIAACMC, which has not been completed.

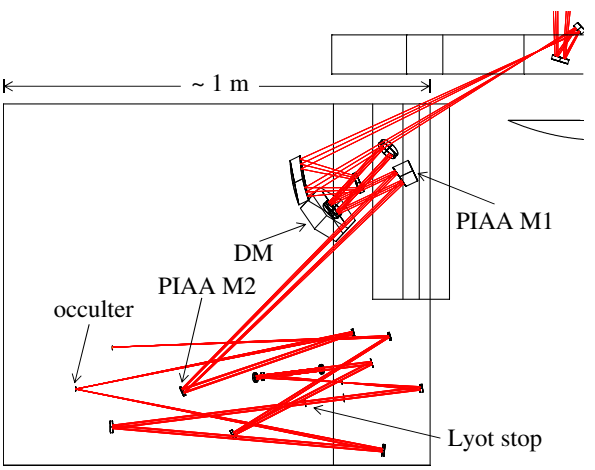

Fig. 1 Gen 2 PIAACMC optical layout. The main differences of this layout to the OMC layout are the lack of a second DM, the lack of pupil relays, beam compression before the occulter to produce a slow beam, and a reflective occulter.

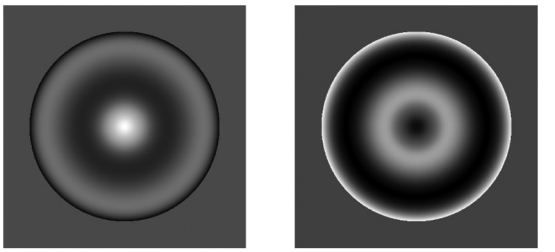

Fig. 2 Nonconic components of Gen 2 PIAA mirror shapes: (a) M1 and (b) M2. The $P-V$ deviation from a conic surface is 2.1 μm.

The Gen 2 PIAACMC occulting mask is completely reflective, with a profiled surface giving rise to phase variations that are integral to the PIAACMC coronagraphic operation. The details of this mask are what compose the bulk of Secs. 3 through 6. Notably, to operate broadband, the first-order notion of the PIAACMC operation requires a mask that has a uniform nonunity amplitude and π phase shift for all wavelengths, and whose diameter scales linearly with wavelength. This is accomplished by something analogous to pulse-width modulation of the phase shift over sub-λ/D spatial scales.

3 Phase-Induced Amplitude Apodization Complex Mask Coronagraph Performance Overview

The main differentiator in performance between PIAACMC and OMC is the small IWA of PIAACMC, more than a factor of 2× smaller than for OMC ($1.3\lambda/D$ compared to $\sim 3\lambda/D$). In addition to simply increasing the "search space" for planets, at smaller IWA there are more planets at less extreme contrasts (easier to observe) and for whom the observed planet flux is higher. Taken together, at smaller IWA there are more targets whose contrasts are easier to observe in a shorter time. A scatter plot of planets known from radial velocity (RV) observations is shown in Fig. 3, where the targets were taken from the same source as in Ref. 5.

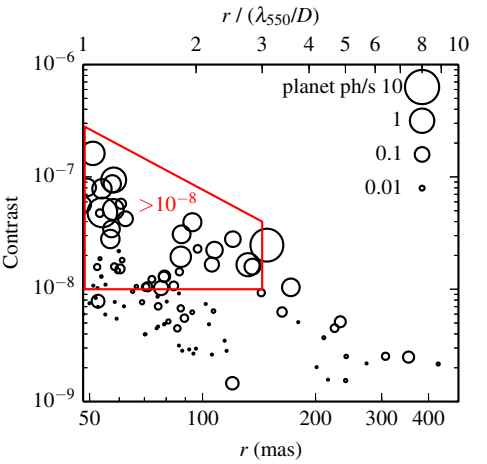

Fig. 3 Contrast of RV planets. Inside of $3\lambda/D$, many planets have contrast $>10^{-8}$ (easier to observe than 10^{-8}). The size of the symbols is a logarithmic representation of observed planet flux, showing that the observable planets at small r have higher observed fluxes. The region outlined in red simply draws attention to bright planets at small separations with contrast $>10^{-8}$.

As can be seen in Fig. 3, there is a large population of planets at $r < 3\lambda/D$ whose contrast is $>10^{-8}$ (less extreme contrast). While 10^{-8} contrast is a threshold for detecting planets at larger separations, at small separations ($r < 3\lambda/D$) many planets can be observed at larger contrasts.

The nominal Gen 2 design, with realistic surface errors on all optics but a perfectly fabricated mask, delivers 24 planets in an observing bandpass of 10% centered at 550 nm, assuming 0.4 mas/axis residual tip-tilt, a 1 mas stellar diameter, and a 30× postprocessing gain factor, as shown in Fig. 4. Also shown in Fig. 4 is the performance of the as-fabricated occulter, characterized as described in detail in Secs. 5 and 6, delivering 15 planets. The performance of the as-fabricated occulter depends strongly on choices made during wavefront control (described in Sec. 6), so this single case study can be taken as a typical example. Relative to the science requirement of 12 planets, this as-fabricated occulter succeeds in meeting the milestone criterion.

4 Fabrication of Gen 2 Phase-Induced Amplitude Apodization Complex Mask Coronagraph Occulting Mask

The Gen 2 PIAACMC occulting mask is all-reflective, with 1259 "zones" of different heights, as shown in Fig. 5. This mask was fabricated at JPL's Microdevices Laboratory (MDL), using polymethyl methacrylate (PMMA) on a Si substrate. The spatial scale at which it was manufactured is identical to that corresponding to the flight design in Sec. 2 and Fig. 1. The height pattern was written onto PMMA using a 100 keV e-beam, with a 70-nm beam size, and 20 nm subpixel size. The PMMA itself can maintain a 60 nm resolution in this context. Because the substrate does not need to transmit light, a Si substrate was chosen, which allows better e-beam performance relative to a glass substrate by offering better electrical and thermal conductivity during e-beam exposure. After e-beam exposure and development of the PMMA, it can be coated with any reflective coating desired. For characterization, aluminum was chosen.

The choice of Al-coated PMMA fabricated at JPL's MDL has flight heritage with Mars Reconnaissance Orbiter[7] and Moon Mineralogy Mapper.[8]

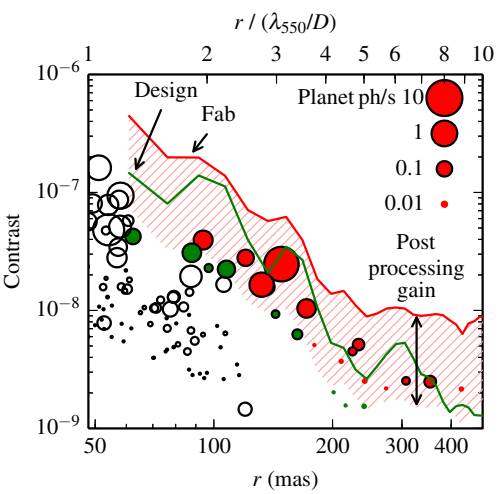

Fig. 4 Contrast performance of two different occulters. The red line is the raw contrast for the as-fabricated occulter, the green line is raw contrast for a perfect occulter. The red symbols are planets observable with postprocessing on the as-fabricated or the perfect occulter, the green symbols are observable only with the perfect occulter. The red hatched region shows the deepest region where SNR = 5 is possible with a 30× postprocessing gain.

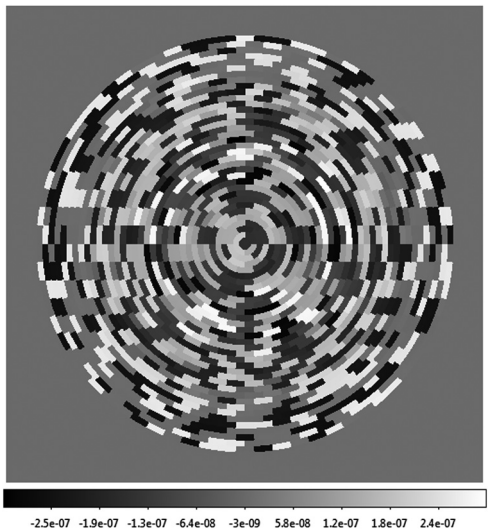

Fig. 5 Gen 2 PIAACMC occulting mask surface heights. The $P - V$ height is 611 nm. There are 35 annular rings, each 2.2-μm wide, with a total diameter 155 μm ($2.9\lambda/D$ at $\lambda = 550$ nm), comprising 1259 height zones. The reflectivity of the mask is uniform everywhere.

5 Characterization of Gen 2 Phase-Induced Amplitude Apodization Complex Mask Coronagraph Occulting Mask

Adequate characterization of the occulting mask requires measuring heights at a wide range of spatial scales. The relevant scales include the details of the transition region between zones at the 10 s of nm level, the heights of zones spanning 2 μm each laterally and extending tens of zones on a side, and heights across the nominally flat region outside the zones extending for ~1 mm. No single characterization technique measures heights accurately at all of these spatial scales, so a combination of techniques is required for this exercise. The relevant measurement instruments are a scanning electron microscope (SEM), a tapping atomic force microscope (AFM), and a ZeMapper interferometric optical microscope. A comparison of these instruments is shown in Table 1.

The characterization scheme used to measure on all these scales is to rely on SEM measurements to estimate the edge transitions (smallest scales, 50 nm to 10 μm), AFM for heights of individual zones (intermediate scales, 1 to 100 μm), and ZeMapper for the surrounding areas (largest scales, 10 μm to 1 mm).

5.1 *Scanning Electron Microscope Characterization (50 nm to 10 μm)*

The SEM has ~20 nm spatial resolution, much finer than the 200 nm design pixels on which the heights are specified. The SEM, viewing the mask at an angle, is good at identifying the characteristic slopes of the transition edges, but has difficulty quantifying heights of the uniform regions. A sample of an edge transition, showing the steep walls between zones, is shown in Fig. 6.

Table 1 Relative strengths and inadequacies of measurement instruments in characterizing relevant spatial scales. The technique that best characterizes each component has been shown in bold.

	Technique			
Component	SEM	Tapping AFM	ZeMapper interferometric optical microscope	
Sharpness of zone transitions ("rounding")	<20 nm **spatial resolution**	200 nm lateral resolution (distorted)	1 μm lateral resolution	Smallest features
Individual zone heights	Hard to quantify features	<6 nm **errors at high-spatial frequencies**	Corrupted by poor lateral resolution	
Wide-angle surrounding features	Hard to quantify features	100 μm distorted FOV, low-order errors	**Good low-order sensitivity for smooth features**	Largest features

The main quantitative result taken from the SEM images is that the walls of the height zones spread by ~60 nm as they transition between zones.

5.2 *Atomic Force Microscope Characterization (1 to 100 μm)*

The AFM measurements, taken in tapping mode, are very good at measuring fine details of heights across a 100 μm 2-D area, but they present some artifacts that must be handled carefully to provide an accurate representation of the sample. The three factors that most affect the measurements are distortion of (x, y) positions, asymmetric errors near steep edges, and low-order height errors.

The distortion is accommodated by fitting the locations of each zone relative to the edge discontinuities. The resolution of the AFM is corrupted near the edges of the zones, so the pixels neighboring the edges are excluded from the measurement of height in each zone. The low-order terms are fit relative to the design, and subtracted. The resulting decomposition is shown in Fig. 7.

The residuals of the zone heights, with respect to the design values, vary by 6 nm rms, which can be compared to the $P-V$ design heights of 611 nm. To give a graphical sense of the relative errors on a uniform scale, a 1-D cut is plotted in Fig. 8.

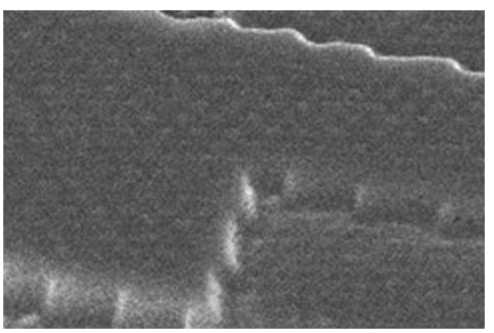

Fig. 6 SEM image of occulting mask. The width of this image is ~6 μm. The individual 200 nm design pixels are clearly visible, and the walls can be seen to spread by ~60 nm.

5.3 *ZeMapper Characterization (10 μm to 1 mm)*

The ZeMapper has the widest FOV of the three measurement techniques, which extends to approximately the limit of the relevant coronagraphic FOV. A representative PIAACMC ZeMapper image (from a separate occulter than the one analyzed here) is shown in Fig. 9. The most prominent feature in the ZeMapper data is the grid pattern. This pattern is due to the field boundaries of the 100 keV e-beam writing pattern, which can only write 0.5 mm squares before repositioning the sample for the next square. The nontelecentric beam illumination treats the edges differently from neighboring square centers. As will be described in Sec. 6, this effect is significant to the performance of the occulter, and should be improved by simple changes in the e-beam parameters.

5.4 *Combination of Characterization Results*

Measurements from these three instruments are all combined to form a single model of the occulter. The propagation models used for high-contrast modeling and wavefront control are paraxial, unfolded models, in which a reflective occulter is represented as having a complex-valued transmission map in the unfolded system.

The characterization measurements are all made at different spatial scales. No single calculation is used to combine all of these scales, but rather, each contributes to the net transmission calculation at its own, separate scale. The net transmission is a simple $t(x, y) = \exp\{2\pi i 2\ S(x, y)/\lambda\}$, a conversion of surface height S to wavefront phase on reflection. The superposition of the components used to generate the full transmission is pictorially represented in Fig. 10.

This decomposition is useful because the final representation of the occulter need not have information at all available spatial frequencies. The system contains a Lyot stop, which imposes a maximum transmitted spatial frequency; all component-wise occulter representations need to contain the correct information up to the maximum transmitted spatial frequency, but may be arbitrarily defined for higher spatial frequencies. This allows Fourier interpolation of the individual patterns, retaining sufficient spatial frequency information in each. This can be done with explicit DFTs with very fine spatial sampling, retaining the frequency information on a coarse grid uniform between patterns, and then using simple FFTs with relatively few elements for propagation.

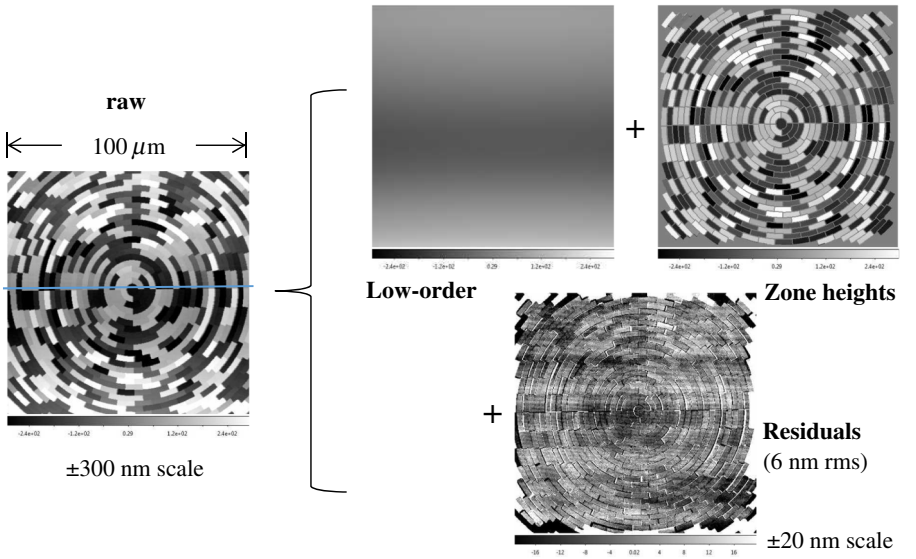

Fig. 7 Decomposition of AFM measurements into components. The left image is the raw AFM measurement, which is corrupted by lateral distortion, poor edge resolution, and low-order height errors. The top-middle image is the low-order fit to the residual heights, the top-right is the design zone heights (a single value over a zone whose location was fit to distortion and whose edges are excluded), and the lower-right image shows the residuals. The sum of the three right-hand images is equal to the left-hand image. The color scale for the residuals is 15× finer than the other components, representing a 6 nm rms. The other three images share a ±300 nm full scale. The blue line through the raw image is the location of the slice shown in Fig. 8.

At the finest scales, the AFM-measured zone heights (without the low-order artifacts) are generated on the design geometry then convolved by a rounding kernel to have the same rounding as measured by the SEM. This produces the first term (AFM + SEM) pictured in Fig. 10, with zero surface height outside of the (rounded) occulter. The ZeMapper data are used exactly pixel-by-pixel as measured, with the occulting pattern itself (where zone heights are nonzero) multiplied by zero. Care must be taken to ensure that no two components have nonzero heights at the same locations, as the superposition of complex transmissions is not valid by surface heights.

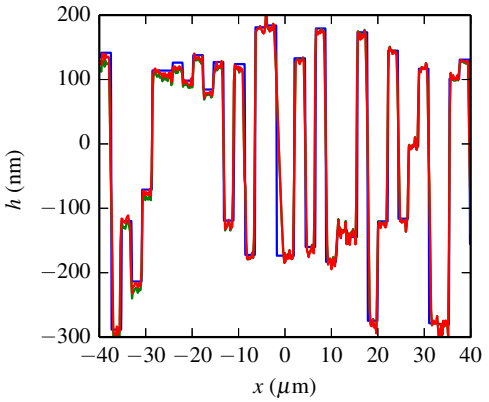

Fig. 8 1-D cut through AFM measurements. The blue line in the "raw" image of Fig. 7 shows the y-location of the cut. The blue line in the plot is the design height, the green line is the raw AFM trace, and the red line is the raw AFM trace minus low-order fit. The mismatch at sharp edges, notably near $x = 0$, is an artifact of the AFM measurement where the tip does not trace steep features. The SEM shows the actual edges to be far sharper than the AFM measurements.

6 Wavefront Control Simulations

The standard optical propagation code used for evaluation of all WFIRST-AFTA coronagraphs has been PROPER.[6,9] The evaluation used here follows the same evaluation framework as all other "official" evaluations, where surface errors are added to each optic except the occulter (true for all coronagraphs). This propagation code (PROPER) is distinct from the wavefront

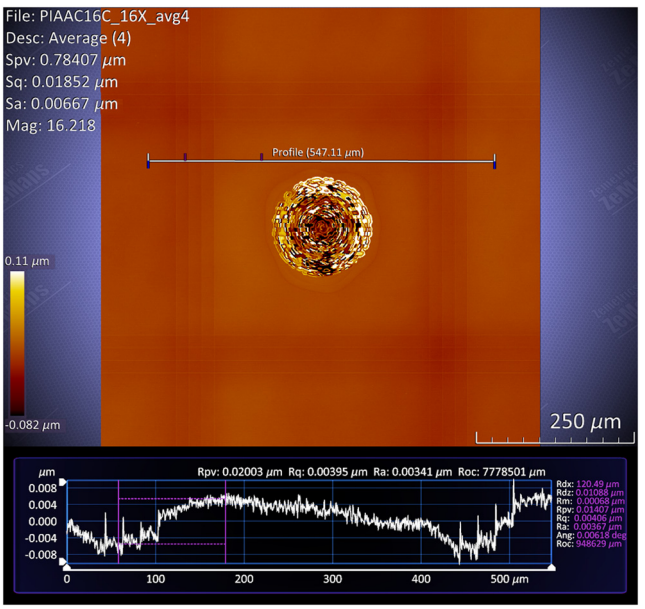

Fig. 9 ZeMapper surface height image. Full scale is 190 nm. The image is ~0.75 mm on a side, which corresponds to about $\pm 8\lambda/D$. The grid pattern comes from the field boundaries of the e-beam writing.

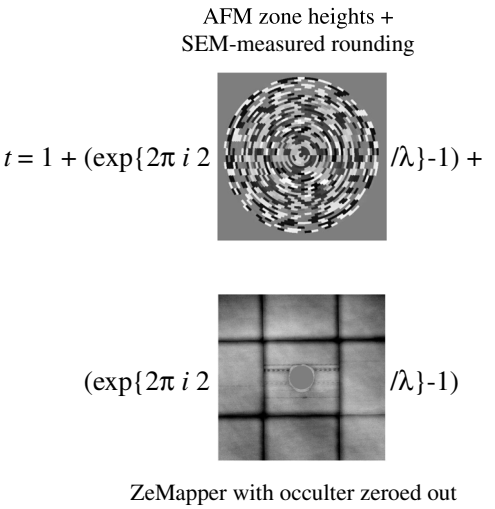

Fig. 10 Pictorial representation of equation incorporating characterization measurements together to form complex "transmission" of reflective occulter.

control code used to solve for DM surfaces. As in Refs. 6 and 9, typical WFIRST-AFTA operational parameters were assumed, most notably the 2.4-m diameter primary mirror with central obscuration and spiders, as well as reflectivity throughputs and camera parameters from Ref. 5, and all evaluations are for a 10% band centered at 550 nm.

The wavefront control code is the same code that is used at JPL's HCIT. The combination of PROPER and the HCIT WFC code are used in a closed loop, where a DM control iteration is passed through PROPER to determine the residual E-field in the image plane, which is then fed to the HCIT WFC code to determine the next DM control iteration. The wavefront control is calculated for a point-source illumination then after wavefront control is complete, the contrast is evaluated with different levels of residual tip-tilt errors and stellar angular diameters. The levels reported here are for 0.4 mas/axis rms residual tip-tilt, and 1 mas stellar angular diameter.

6.1 *Trade Between Wavefront Control and Throughput*

The improvement of contrast as wavefront control progresses involves a trade between better contrast and planet light throughput. It is typically assumed that planet detection will be background-limited, and that only the planet light brighter than the planet half-max intensity is useful for observations. As such, a "core throughput" metric is used where the fraction of planet light brighter than half-max is compared to the total planet light.[6] This core throughput metric is closely related to the Strehl ratio, which specifically characterizes the changes in peak brightness.

The reduction in Strehl ratio is roughly described by the Marechal/Mahajan approximation, $S \sim \exp\{-\Delta^2\}$ where Δ is the rms wavefront variation in radians. The majority of the improvement in contrast is not wavefront "correction," in which the wavefront gets flatter, but rather wavefront control, where the DM forces the PSF into a new distribution. The improvement in contrast comes from the use of more DM stroke, which carries the accompanying loss of Strehl and reduced core throughput.

The final contrast is strongly dominated by residual tip-tilt errors, making the improvements from different wavefront control solutions beyond some point largely irrelevant to the final contrast. A range of wavefront control solutions, evaluated for 0.4 mas/axis residual tip-tilt and a 1-mas diameter star, is shown in Fig. 11 and tabulated in Table 2. In every case, the contrast is a two-dimensional map, but the wavefront control creates a high-contrast region only over 180 deg of the image plane; this two-dimensional contrast is averaged over the intersection of an annulus and the half of the image plane that is controlled, and is plotted as a function of r only.

In Table 2, the total number of planets observable through contrast considerations increases as wavefront control continues, but the throughput (for all planets) decreases. The red line is chosen as the "typical" wavefront control case, where 15 planets are observable, but the throughput has decreased to 55% of that for a perfect as-designed occulter.

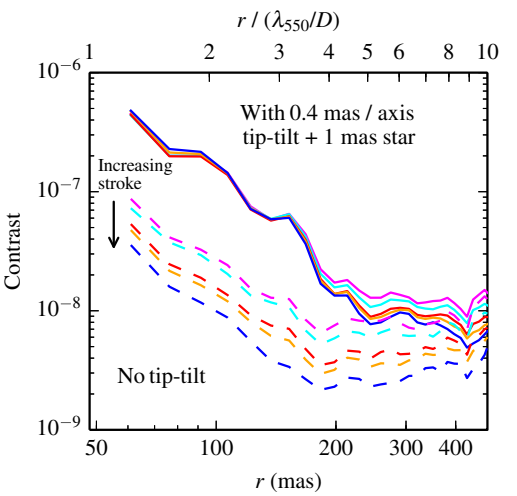

Fig. 11 Contrast using as-fabricated mask for different wavefront control solutions. The colors represent a progression of continued wavefront control, producing increasingly better contrast in the absence of tip-tilt errors (dashed lines), but when residual tip-tilt and 1 mas stellar diameter are included (solid lines) the different wavefront control solutions produce similar small-angle contrast to one another. Increasing stroke produces reduced throughput (shown in Table 2) but more total planets. The red line is referenced as the "typical" wavefront control case throughout this document.

Table 2 Relationship between wavefront control solution, number of planets observed, and throughput. Colors refer to the plots in Fig. 11. Rows are arranged in order of improving contrast.

Color	Number of planets	Throughput relative to design (%)
Magenta	14	65
Cyan	15	60
Red[a]	15	55
Orange	16	51
Blue	16	49

[a]The red curve is the wavefront control solution used for all other quantification, referenced as a "typical" wavefront control solution.

6.2 *Paths to Improvement in Occulter Fabrication*

Evaluating other hypothetical masks for the same considerations of throughput and planet yield, the most promising paths for fabrication improvements can be identified. Figure 12 shows two additional hypothetical improvements and their impact on science yield, tabulated in Table 3.

The two hypothetical cases considered here are for the field boundaries to change in spacing from 0.5 mm squares to 1 mm squares (i.e., the boundaries move farther out in the image plane), and for there to be no errors at all in areas surrounding the zones (i.e., the ZeMapper portion of Fig. 10 is perfectly zero). As can be seen from the throughput and planet yield numbers in Fig. 12 and Table 3, simply moving the positions of the field boundaries improves the planet yield significantly with a modest improvement in throughput. Removing all of the errors surrounding the zones delivers a performance quite close to the perfect occulter, meaning that the zone errors alone are quite easy to correct with wavefront control.

The consideration of changing the field boundaries from 0.5 mm squares to 1 mm squares is motivated by the 50 keV writing capability of the e-beam at JPL. The existing mask was exposed at 100 keV, which has a 0.5 mm field boundary limit. The 50 keV writing mode has a 1 mm field boundary limit, but was unavailable at the time of the occulter fabrication because a component required for alignment at 50 keV was not functioning. The identification of the field boundary size as a limiting factor was not made until recently, so the 50 keV experiment was deferred to the next round of PIAACMC mask fabrication.

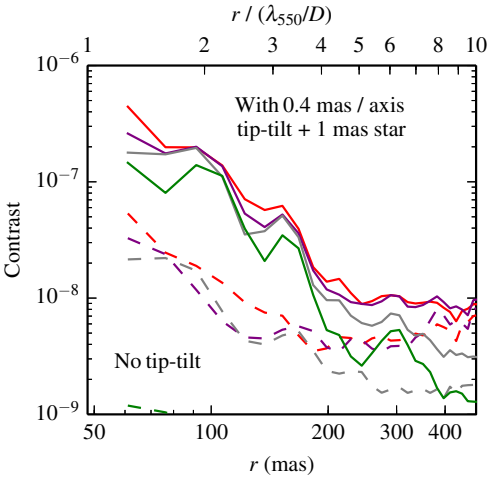

Fig. 12 Contrast of typical wavefront control solution on as-fabricated occulter (red), perfect as-designed occulter (green), and two hypothetical fabrication improvements. The dashed lines are without tip-tilt errors, the solid lines are with residual tip-tilt errors and 1 mas stellar diameter.

Table 3 Planet yield and throughput for four mask assumptions: the as-fabricated mask, two hypothetical treatments of errors, and the design mask.

Mask	Color	Number of planets	Throughput relative to design (%)
As-fabricated	Red	15	55
Field boundaries at 1 mm	Magenta	20	62
No errors outside of zones	Gray	21	91
Design	Green	24	100

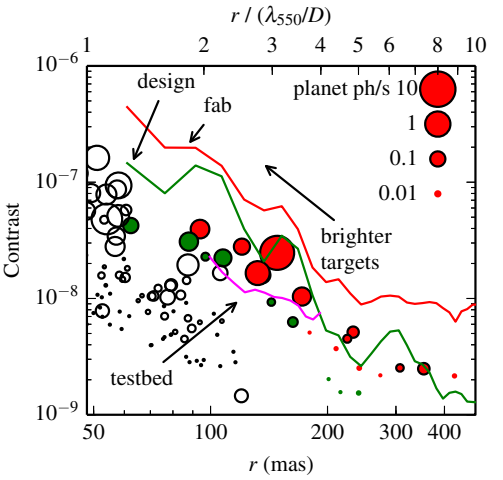

Fig. 13 RV planets plotted against nominal solution for as-fabricated occulter and as-designed occulter. Previous HCIT testbed results from an unobscured 10% broadband demonstration (at 800 nm) are shown in magenta. Planets observable with 30× postprocessing are shown in red, green planets cannot be observed by the as-fabricated occulter but can be observed by the as-desgined occulter.

6.3 *Small Inner Working Angle Targets and Past Testbed Results*

The contrast plots of Figs. 11 and 12 are shown without the RV planets overlaid, due to the crowding associated with several lines shown on each plot. Taking the typical wavefront control solution on the as-fabricated occulter, and the perfect as-designed occulter, the RV planets are overlaid in Fig. 13.

What is notable about Fig. 13 is that the planets at small angles, $<3\lambda/D$, have much brighter observed fluxes than those farther out, on the order of 10× to 100×. The advantage of PIAACMC having a small IWA is that these planets may be observed, which makes the observing scenario far more appealing because high-SNR measurements can be made in a short time.

Figure 13 shows a contrast curve from a previous testbed demonstration.[4] This curve is not directly comparable, because it used an unobstructed pupil and a PIAA coronagraph without the PIAACMC occulter (but with a simple hard-edged occulter). It was also measured in a 10% band centered at 800 nm, rather than the 10% at 550 nm shown for Gen 2 model results.

7 Conclusion

The results presented here describe a PIAACMC occulting mask fabricated at JPL's MDL. This mask, the first PIAACMC mask ever fabricated on PMMA, is modeled to deliver contrast yielding 15 RV planets (typically), exceeding the science requirement of 12 planets. This performance appears to be dependent on the e-beam field boundaries, which have a ready path for improvement, by utilizing the 50 keV writing mode of the existing e-beam facility at JPL.

What may be surprising is that the 1259 zone heights determined in the design were not particularly challenging to fabricate sufficient tolerances by this technique—while it appears complicated, it is well within the MDL fabrication capability. The first attempt to fabricate such an occulter delivered rms zone height errors of just 1% of the $P-V$ zone heights, clearly sufficient for 10% broadband coronagraphic operation.

Since the time of the analysis presented in this paper, a new PIAACMC design has been produced. This design, called "Gen 3," has its tip-tilt sensitivity reduced by 10 to 15× compared with the Gen 2 design analyzed in this paper.[5,6] In Ref. 6, the Gen 3 design is described both as the "revised" PIAACMC design and as "PIAACMC 20150322." The mask for the Gen 3 design is somewhat simplified compared with the Gen 2 mask, using only 505 zones as compared with 1259 zones for Gen 2. This is due to improvements in the mask optimization algorithm, and produces a mask with more favorable feature sizes compared with the Gen 2 mask. No Gen 3 masks have yet been fabricated or characterized, so no analysis comparable to that presented in this paper has been performed on a Gen 3 mask to date. Testbed validation of the Gen 2 mask analysis presented here will not be pursued, rather the Gen 3 masks will be fabricated, characterized, and tested in the laboratory.

The modeling results do depend strongly on the assumed residual tip-tilt seen by the coronagraph. The 0.4 mas rms/axis residual tip-tilt shown here is somewhat optimistic. Since the time of this analysis, more modeling has been done on the expected residual tip-tilt[10] for WFIRST-AFTA, producing a current estimate of 0.5 mas rms/axis. The analysis presented here has not been repeated for the updated residual tip-tilt estimate, as the Gen 3 design improvements and greatly reduced tip-tilt sensitivity make the Gen 2 design less appealing as a flight baseline. In essence, the performance expectations presented in this paper can be considered overly pessimistic compared with Gen 3 performance.

Acknowledgments

This research was carried out at the Jet Propulsion Laboratory, California Institute of Technology, under a contract with the National Aeronautics and Space Administration.

References

1. M. Charles Noecker et al., "Coronagraph instrument for WFIRST-AFTA," in press.
2. O. Guyon, "Imaging earth-like planets around late-type stars with low-inner working angle PIAA coronagraphy," *Proc. SPIE* **8864**, 886414 (2013).
3. Brian Kern et al., "Laboratory demonstration of phase induced amplitude apodization (PIAA) coronagraph with better than 10-9 contrast," *Proc. SPIE* **8864**, 88640R (2013).
4. O. Guyon et al., "Technology development for exoplanet missions, technology milestone report: phase-induced amplitude apodization (PIAA) technology development, milestone 3–10% bandpass contrast demonstration," 20 May 2014, http://exep.jpl.nasa.gov/technology/Guyon-PIAA-Milestone-3.pdf (19 January 2016).
5. W. A. Traub et al., "Science yield estimate with the WFIRST-AFTA coronagraph," in press.
6. J. E. Krist and B. Nemati, "Numerical modelling of the proposed WFIRST-AFTA coronagraphs and their predicted performances," *J. Astron. Telesc. Instrum. Syst.* **2**(1), 011003 (2015).
7. D. W. Wilson et al., "Recent advances in blazed grating fabrication by electron-beam lithography," *Proc. SPIE* **5173**, 115 (2003).
8. R. O. Green et al. "The moon mineralogy mapper (M3) imaging spectrometer for lunar science: instrument description, calibration, on-orbit measurements, science data calibration and on-orbit validation," *J. Geophys. Res.* **116**, E00G19 (2011).
9. J. E. Krist, "PROPER: an optical propagation library for IDL," *Proc. SPIE* **6675**, 66750P (2007).
10. B. Kern, "Impact of WFIRST-AFTA line-of-sight jitter distributions on PIAACMC science yield," *J. Astron. Telesc. Instrum. Syst.* **2**(1), 011016 (2016).

Biographies for the authors are not available.